Photonic Crystals with Split Ring Unit Cells for Subwavelength Light Confinement

KELLEN P. ARNOLD,[1] SAMI I. HALIMI ,[2] JOSHUA A. ALLEN,[1] SHUREN HU,[2] SHARON M. WEISS,[1,2,*]

[1]*Interdisciplinary Materials Science Program, Vanderbilt University, Nashville, TN 37235, USA*
[2]*Department of Electrical Engineering and Computer Science, Vanderbilt University, Nashville, TN 37235, USA*
**Corresponding author: sharon.weiss@vanderbilt.edu*

Received 10 Month 2021; revised XX Month, XXXX; accepted XX Month XXXX; posted XX Month XXXX (Doc. ID XXXXX); published XX Month XXXX

Here we report a photonic crystal with a split ring unit cell shape that demonstrates an order of magnitude larger peak electric field energy density compared to a traditional photonic crystal. Split ring photonic crystals possess several subwavelength tuning parameters, including split ring rotation angle and split width, which can be leveraged to modify light confinement for specific applications. Modifying the split ring's parameters allows for tuning of the peak electric field energy density in the split by over one order of magnitude and tuning of the air band edge wavelength by nearly 10 nm in the near infrared region. Designed to have highly focused optical energy in an accessible subwavelength gap, the split ring photonic crystal is well-suited for applications including optical biosensing, optical trapping, and enhanced emission from a quantum dot or other nanoscale emitter that could be incorporated in the split.

The study of photonic crystals (PhCs) over the past three decades has led to improved understanding of optical phenomena at the micro and nanoscale while at the same time advancing the capabilities of a wide range of optical devices that rely on strong-light matter interaction. Strategic engineering of the periodic dielectric structure of PhCs and inclusion of defects to form waveguides and cavities has led to precise tailoring of the modal [1,2] and dispersive properties [3,4] of PhC structures. Among the notable PhC-based devices that have been demonstrated are PhC lasers [5–7], electro-optic modulators [8–10], optical biosensors [11,12], and solar cells [13–15].

Recent work has revealed that the specific geometry of a PhC unit cell has a strong influence on the local electric field and energy distributions. For example, adding a vertical dielectric bar, referred to as an antislot, to a circular unit cell was shown to change the energy distribution from being relatively uniform across the unit cell to becoming highly localized in the antislot [16,17]. In another example, a bowtie-shaped unit cell was demonstrated in experiment to support extremely high energy density at the knot of the bowtie [18]. Prior work has also shown that a mix and match approach can be applied to PhC design wherein different unit cell shapes (e.g., antislots and bowties) can be combined in a single PhC nanobeam to achieve an even higher level of control of the mode profile without sacrificing the quality factor (Q) of the PhC [2]. These examples of redistribution of light in PhC unit cells can be explained using fundamental electromagnetic principles [16,17]; hence, other strategic unit cell shapes could be employed to realize desired field distributions that are favorable for specific applications.

In this Letter, we investigate the properties and design freedoms enabled by a silicon split ring-shaped PhC unit cell. Analogous to the shared electric field confinement of plasmonic bowties [19] and dielectric PhC bowtie unit cells [18] for which light is localized at the knot of the bowtie, we demonstrate that the peak electric field energy density in a split ring PhC unit cell is located in the narrow split region, similar to the case for a split ring metamaterial [20]. It is important to note that although the resulting electric field localization may be similar, and in both cases is dependent on the orientation of the split ring relative to the polarization of light, the mechanism of the field localization is different between plasmonics, metamaterials, and PhCs [18–20]. While metallic metamaterial split rings rely on plasmonic coupling in the resonator array, dielectric PhC split rings redistribute the field according to electromagnetic interface conditions inside the unit cell. Moreover, while metallic split ring metamaterials can enable new effective materials properties including negative permittivity that are not possible in dielectric split ring PhCs, dielectric split rings are low loss, enabling incorporation in high Q cavities with in-plane light confinement for on-chip applications, which is not possible with split ring metamaterials due to their large optical losses. Through finite-difference time domain (FDTD) analysis, we calculate the energy distribution in a silicon split ring PhC as a function of the rotation angle of the unit cell and we quantify the peak energy density in the split as a function of the geometry and rotation of the split ring unit cell. By achieving more than a 10-fold enhancement of the electric field energy density in the split compared to a traditional circular PhC unit cell (air mode), the split ring PhC offers significant advantages for optical biosensing, optical trapping, and applications requiring strong light-matter interaction within an air region.

A schematic of the split ring PhC is shown in Fig. 1(a). The localized energy inside the split is illustrated by the pink glow and is quantified in simulations presented below. The tunable dimensions of the split ring PhC unit cell are shown in Fig. 1(b) and are: split width (w_s), inner ($r_{C,\,inner}$) and outer ($r_{C,\,outer}$) radius of the dielectric "C" comprising the split ring, radius of the containing air hole (r_{air}), and rotation angle of the split ring (θ). In this work, we consider a suspended silicon split ring PhC waveguide in air due to the computational efficiency of studying a structure that is symmetric in the out-of-plane dimension. Importantly, the general trends

analyzed for the suspended split ring PhC also apply to split ring PhCs fabricated on silicon-on-insulator wafers and can be leveraged for the design of split ring PhC cavities.

Three-dimensional finite difference time domain (FDTD) methods were conducted using Ansys Lumerical software. For all simulations unless otherwise stated, the period of the split ring unit cells is 390 nm, the waveguide width is 750 nm, and the split ring parameters are: $w_s = 10$ nm, $r_{C,inner} = 50$ nm, $r_{C,outer} = 70$ nm, $r_{air} = 90$ nm, and $\theta = 0^\circ$ (i.e., R0 unit cell). For comparison, the properties of a circular air hole PhC with a period of 390 nm, waveguide width of 750 nm, and air hole radius of 90 nm (i.e., same dimensions as the split ring PhC but without the silicon split ring included inside the air hole) were simulated.

First, the photonic band structure of an infinitely long split ring PhC nanobeam was calculated for the fundamental transverse electric (TE) mode. Due to computational limitations, a 5 nm mesh step was utilized in the in-plane *x*- and *y*-directions covering the extent of the unit cell. Non-uniform conditions were utilized in the out-of-plane *z*-dimension and in the silicon region outside the air hole with a maximum mesh cell step of ~35 nm at the outer edge of the simulation region. As shown in Fig. 2(a), the photonic band gap extends from ~166 to 187 THz (~1605 to 1805 nm) and the TE band extent remains quite wide upon inclusion of the split ring into the PhC unit cell. The higher frequency air band is of particular importance for the split ring PhC; light confinement in the split requires energy localization in the air hole regions of the PhC to enable the silicon split ring to redistribute the energy within the unit cell according to electromagnetic interface conditions [16].

The transmission spectrum of a finite length PhC nanobeam with 27 split ring unit cells was also calculated. For this simulation, a TE modal source with bandwidth 1500 to 1630 nm was used for excitation and a transmission monitor was placed at the output of the split ring PhC nanobeam. A 2.5 nm mesh step in the *x* and *y*-directions was utilized across all unit cells. As shown in Fig. 2(b), the transmission spectrum is characterized by a photonic bandgap between approximately 1603 and 1813 nm. The slight differences in the air and dielectric band edge locations between the transmission simulation and band structure calculation are due to differences in the meshing between the two simulations. We note that the air band edge for the comparison circular air hole PhC is located near 1550 nm; hence, the addition of the silicon split ring in the unit cell red-shifts the transmission spectrum, as expected, without significantly changing the extent of the bandgap.

With the band edge locations identified, we next calculated the mode profile inside the split ring PhC unit cell at the air band edge frequency using TE dipole excitation and a 1 nm mesh step. Using periodic boundary conditions across the *x*-direction, the simulated PhC waveguide is modeled as infinitely long. This calculation was repeated for multiple rotation angles. We note that in order to accurately assess how the rotation angle of the split ring affects light redistribution within the unit cell, the power emitted by the dipole source should be the same for all unit cell configurations. Typically, the power that is emitted by a dipole source is dependent on the environment surrounding the dipole (i.e., via the Purcell effect) [21].

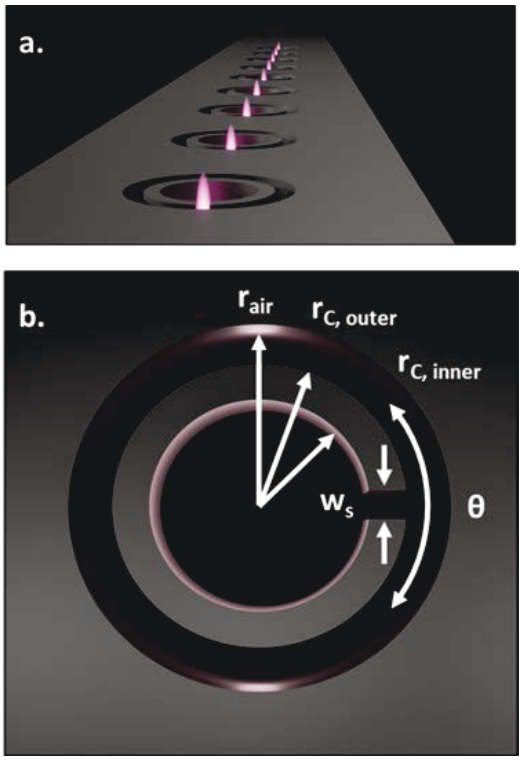

Fig. 1. (a) Illustration of silicon split ring PhC nanobeam. The silicon waveguide is shaded in grey and the air regions indicated by void (black). The area of light localization in the R0 split ring PhC is illustrated by the pink glow inside the split in each ring. (b) Schematic of split ring PhC unit cell with tunable dimensions labeled.

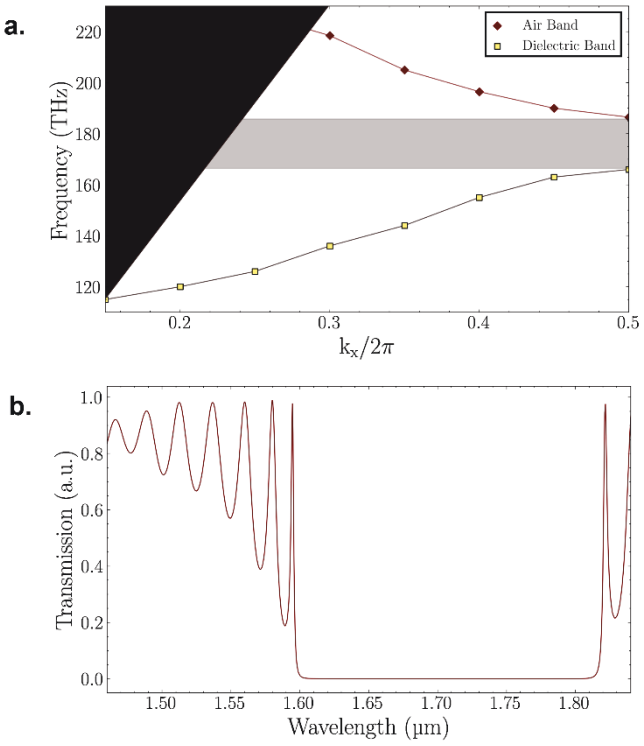

Fig. 2. (a) Photonic band structure of R0 split ring PhC showing air band (red diamond) and dielectric band (yellow square). The light line above which no guided modes propagate in a PhC is shaded in black. The extent of the TE photonic band gap is shaded in grey. (b) Simulated transmission spectrum for split ring PhC having a finite length of 27 unit cells.

Therefore, in our analysis of the electric fields recorded by the field monitors in simulations, we divide the square of the electric field by the Purcell factor returned by the simulation to normalize the power emitted from the dipole to be constant across all simulations. Appropriate apodization conditions are also utilized to ensure that only light coupling to the desired air mode is considered. Thus, we obtain a strict comparison of the energy density differences for various parameter changes that may be applied to the design of cavities and other resonators. Figure 3 shows the energy density (proportional to E^2) distribution at the air band edge of the R0, R30, R60, and R90 split ring unit cells normalized to the peak energy density in the R0 unit cell (E_{R0}^2). The peak energy density in the unit cell drops by ~40% as the split ring angle is varied from zero to ninety degrees, and the location of peak energy density transitions from being well-confined inside the split to being spread out along the upper and lower air ring regions. To understand the rotation-dependent energy distributions, we first closely examine the R0 and R90 split ring unit cells. For the R0 unit cell, the TE-polarized electric field that oscillates in the plane across the waveguide width (*y*-direction) directly crosses the vertical silicon-air-silicon interfaces of the split. Electromagnetic interface conditions dictate that the normal component of the electric field is discontinuous across an interface (i.e., scaled by the ratio of the electric permittivities of the two dielectric materials at the interface). Since the electric field is normal to these silicon/air interfaces, the electric field amplitude in the air slot of the R0 split ring PhC unit cell is enhanced by the ratio of the silicon and air permittivities - this effect is known as the slot effect [22]. We note that the lower electric field energy density present in the air regions toward the top and bottom of the unit cell between the outer edge of the silicon ring and silicon region outside the air hole can also be explained by electromagnetic interface conditions; the electric field enhancement in these air regions is much lower than in the split due to their much larger width [22]. Conversely, for the R90 split ring unit cell, TE-polarized light is tangential to the silicon-air-silicon interfaces of the split. Therefore, since electromagnetic interface conditions dictate that the tangential component of the electric field is continuous across an interface, there is no electric field enhancement in the split of the R90 split ring unit cell. Accordingly, the peak electric field energy density in the R90 split ring unit cell is located in the air regions toward the top and bottom of the unit cell between the outer edge of the silicon ring and silicon region outside the air hole. Without light localization in the split, the peak energy density in the R90 split ring unit cell is nearly the same as that in a unit cell with a full ring having no split (see supplemental document Fig. S1 for details). With the understanding that the energy distributions for the R0 and R90 split ring PhC unit cells are largely governed by electromagnetic interface conditions, we can now explain the energy distributions of the split ring PhC unit cells with intermediate rotation angles. For the unit cells with rotation angle greater than 0°, the energy density enhancement scales with the sine of the rotation angle (i.e., by considering the horizontal component of the silicon/air interface). Figure 3(e) quantifies the peak energy density in the split as a function of rotation angle, normalized to the peak energy density in the R0 unit cell. In comparison to the traditional circular air hole PhC, the peak energy density in the split of the R0 split ring PhC is 10-times higher (see Fig. S2). Notably, the peak energy density inside the split diminishes by greater than one order of magnitude

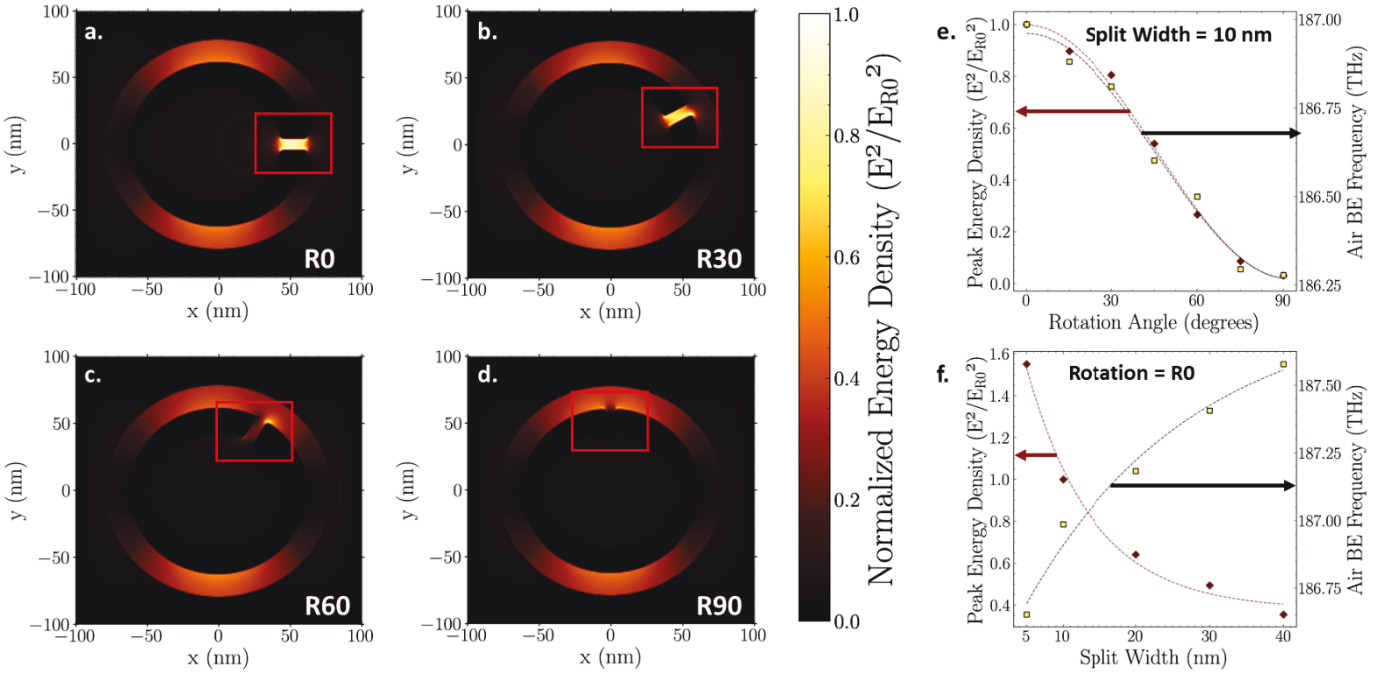

Fig. 3. Electric field energy density (i.e., proportional to E^2) distribution at air band edge for (a) R0, (b) R30, (c) R60, and (d) R90 split ring PhC unit cells using a color map normalized to the peak energy density of the R0 unit cell (E^2/E_{R0}^2), allowing direct comparison across all unit cells. (e) Rotation angle dependence of peak energy density (normalized to E_{R0}^2) inside split ring PhC unit cell (red diamonds) and air band edge (BE) frequency (yellow squares); the split width is held constant at 10 nm. (f) Split width dependence of peak energy density (normalized to E_{R0}^2) and air band edge (BE) frequency; the rotation angle is held constant at zero degrees.

from R0 to R90, offering tunability of electric field strength and location from inside the well-localized split (R0) to the surrounding airhole (R90). Such tunability could be advantageous for PhC cavity applications for which a large difference in peak energy density is desirable in adjacent unit cells (e.g., optical trapping); prior work demonstrated that PhC cavities can be formed by appropriately rotating asymmetric unit cells to taper the mirror strength along the nanobeam [16]. The maximum energy enhancement achievable in the split ring PhC falls between that of an air mode circular air hole PhC and a bowtie PhC. Moreover, the maximum energy enhancement is similar to that achievable in an antislot PhC with an added air slot (i.e., split) of similar width to that of the split ring [16]. Application-specific requirements dictate which geometry is most advantageous, considering the potential tradeoffs between fabrication complexity, peak electric field energy density, spatial extent of the highest energy region, and design degrees of freedom.

Figure 3(e) also shows the change in air band edge frequency for the split ring PhCs with different rotation angles. As expected, the air band edge position scales similarly to the peak energy density, as a function of the rotation angle; as less light is localized in the air split, the air band edge frequency decreases. The air band edge frequency decreases by 0.75 THz from R0 to R90, which corresponds to an approximate increase of 10 nm in wavelength in the near infrared.

Finally, we examine how changing the split width affects the energy density and air band edge frequency, using similar methods to the calculations described above that investigated the effect of the rotation angle of the split ring. Fig. 3(f) shows that as the split width increases, the peak energy density decreases, following from the slot-effect. The peak energy density scales by a factor of nearly four as the split width changes from 5 and 40 nm. The change in peak energy density is greatest for 5 – 20 nm split widths because as the split width increases to a larger dimension than that between the ring edge and surrounding waveguide $(r_{air} - r_{C,outer})$ (i.e., $w_s > 20$ nm), the location of the peak energy density moves from the split to the top and bottom air regions of the unit cell. Figure 3(f) also shows that the air band edge frequency increases by 1 THz as the slot width increases from 5 – 40 nm. This is predicted by the filling fraction because the volume of silicon decreases in the unit cell when the split width increases. Fabrication capabilities determine the smallest achievable split width. We note, as guided by the trends, that a split ring PhC cavity could be formed by appropriately varying the split width of split ring unit cells along a PhC nanobeam; this represents a unique degree of freedom offered by the asymmetry present in the split ring unit cell. We further note that other degrees of freedom in the split ring unit cell, including the width of the silicon split ring and the radius of the air hole, could be varied to achieve PhC cavities.

In summary, we present a new PhC unit cell with a split ring shape that supports low-loss, subwavelength confinement of the electric field in air. The asymmetry of the split ring PhC unit cell offers several tuning parameters, including rotation angle, split width, and split ring width, that can be used to control the air band edge frequency and electric field profile. With these additional degrees of freedom we show for the first time that it is possible to move an optical "hot spot" at any location within the PhC unit cell, rather than being limited to the center of a waveguide [22], PhC unit cell [18], or dielectric region between PhC unit cells [23]. With a split width of 10 nm and rotation angle of 0^o, the split ring PhC demonstrates a 10-fold enhancement of the electric field energy density over traditional circular air hole PhCs. Appropriate selection of the tunable parameters of the split ring PhC make it an attractive option for particle-field interactions in optical trapping or sensing platforms. Together with other recently reported subwavelength-engineered PhC unit cell designs such as the bowtie and antislot, split ring unit cells expand the design space for achieving a highly tailorable mode profile, customizable for desired applications.

Funding. National Science Foundation (NSF) (ECCS1809937).

Acknowledgments. The Vanderbilt Advanced Computing Center for Research and Education (ACCRE) is acknowledged for simulation resources and technical support. The authors thank F. O. Afzal and L. D. Ryder for useful technical discussions.

Disclosures. The authors declare no conflicts of interest.

Data availability. Data underlying the results presented in this paper are not publicly available at this time but may be obtained from the authors upon reasonable request.

Supplemental document. See Supplement 1 for supporting content.

References

1. L. H. Frandsen, Y. Elesin, L. F. Frellsen, M. Mitrovic, Y. Ding, O. Sigmund, and K. Yvind, Opt. Express **22**, 8525 (2014).
2. S. I. Halimi, Z. Fu, F. O. Afzal, J. A. Allen, S. Hu, and S. M. Weiss, J. Opt. Soc. Am. B **37**, 3401 (2020).
3. T. Baba, Nat. Photonics **2**, 465 (2008).
4. H. Kurt and D. S. Citrin, Opt. Express **13**, 10316 (2005).
5. T. Zhou, M. Tang, G. Xiang, B. Xiang, S. Hark, M. Martin, T. Baron, S. Pan, J. S. Park, Z. Liu, S. Chen, Z. Zhang, and H. Liu, Nat. Commun. **11**, 977 (2020).
6. K. Takeda, T. Sato, T. Fujii, E. Kuramochi, M. Notomi, K. Hasebe, T. Kakitsuka, and S. Matsuo, Opt. Express **22**, 702 (2015).
7. G. Crosnier, D. Sanchez, S. Bouchoule, P. Monnier, G. Beaudoin, I. Sagnes, R. Raj, and F. Raineri, Nat. Photonics **11**, 297 (2017).
8. M. Li, J. Ling, Y. He, U. A. Javid, S. Xue, and Q. Lin, Nat. Commun. **11**, 4123 (2020).
9. Y. Terada, K. Kondo, R. Abe, and T. Baba, Opt. Lett. **42**, 5110 (2017).
10. H. Yan, X. Xu, C.-J. Chung, H. Subbaraman, Z. Pan, S. Chakravarty, and R. T. Chen, Opt. Lett. **41**, 5466 (2016).
11. G. A. Rodriguez, P. Markov, A. P. Cartwright, M. H. Choudhury, F. O. Afzal, T. Cao, S. I. Halimi, S. T. Retterer, I. I. Kravchenko, and S. M. Weiss, Opt. Express **27**, 9536 (2019).
12. H. Inan, M. Poyraz, F. Inci, M. A. Lifson, M. Baday, B. T. Cunningham, and U. Demirci, Chem. Soc. Rev. **46**, 366 (2017).
13. S. Bhattacharya and S. John, APL Photonics **5**, 020902 (2020).
14. D. Zhou and R. Biswas, J. Appl. Phys. **103**, 093102 (2008).
15. A. Chutinan, N. P. Kherani, and S. Zukotynski, Opt. Express **17**, 8871 (2009).
16. S. Hu and S. M. Weiss, ACS Photonics **3**, 1647 (2016).
17. H. Choi, M. Heuck, and D. Englund, Phys. Rev. Lett. **118**, 223605 (2017).
18. S. Hu, M. Khater, R. Salas-Montiel, E. Kratschmer, S. Engelmann, W. M. J. Green, and S. M. Weiss, Sci. Adv. **4**, eaat2355 (2018).
19. D. P. Fromm, A. Sundaramurthy, P. J. Schuck, G. Kino, and W. E. Moerner, Nano Lett. **4**, 957 (2004).
20. D. R. Smith, W. J. Padilla, D. C. Vier, S. C. Nemat-Nasser, and S. Schultz, Phys. Rev. Lett. **84**, 4184 (2000).
21. J. Riedrich-Möller, C. Arend, C. Pauly, F. Mücklich, M. Fischer, S. Gsell, M. Schreck, and C. Becher, Nano Lett. **14**, 5281 (2014).
22. V. R. Almeida, Q. Xu, C. A. Barrios, and M. Lipson, Opt. Lett. **29**, 1209 (2004).
23. J. D. Ryckman and S. M. Weiss, Appl. Phys. Lett. **101**, 071104 (2012).

References

1. L. H. Frandsen, Y. Elesin, L. F. Frellsen, M. Mitrovic, Y. Ding, O. Sigmund, and K. Yvind, "Topology optimized mode conversion in a photonic crystal waveguide fabricated in silicon-on-insulator material," Opt. Express 22(7), 8525–8532 (2014).
2. S. I. Halimi, Z. Fu, F. O. Afzal, J. A. Allen, S. Hu, and S. M. Weiss, "Controlling the mode profile of photonic crystal nanobeam cavities with mix-and-match unit cells," J. Opt. Soc. Am. B 37(11), 3401–3406 (2020).
3. T. Baba, "Slow light in photonic crystals," Nat. Photonics 2(8), 465–473 (2008).
4. H. Kurt and D. S. Citrin, "Annular photonic crystals," Opt. Express 13(25), 10316–10326 (2005).
5. T. Zhou, M. Tang, G. Xiang, B. Xiang, S. Hark, M. Martin, T. Baron, S. Pan, J. S. Park, Z. Liu, S. Chen, Z. Zhang, and H. Liu, "Continuous-wave quantum dot photonic crystal lasers grown on on-axis Si (001)," Nat. Commun. 11(1), 977–983 (2020).
6. K. Takeda, T. Sato, T. Fujii, E. Kuramochi, M. Notomi, K. Hasebe, T. Kakitsuka, and S. Matsuo, "Heterogeneously integrated photonic-crystal lasers on silicon for on/off chip optical interconnects," Opt. Express 22(26), 702–708 (2015).
7. G. Crosnier, D. Sanchez, S. Bouchoule, P. Monnier, G. Beaudoin, I. Sagnes, R. Raj, and F. Raineri, "Hybrid indium phosphide-on-silicon nanolaser diode," Nat. Photonics 11(5), 297–300 (2017).
8. M. Li, J. Ling, Y. He, U. A. Javid, S. Xue, and Q. Lin, "Lithium niobate photonic-crystal electro-optic modulator," Nat. Commun. 11(1), 4123–4130 (2020).
9. Y. Terada, K. Kondo, R. Abe, and T. Baba, "Full C-band Si photonic crystal waveguide modulator," Opt. Lett. 42(24), 5110–5112 (2017).
10. H. Yan, X. Xu, C.-J. Chung, H. Subbaraman, Z. Pan, S. Chakravarty, and R. T. Chen, "One-dimensional photonic crystal slot waveguide for silicon-organic hybrid electro-optic modulators," Opt. Lett. 41(23), 5466–5469 (2016).
11. G. A. Rodriguez, P. Markov, A. P. Cartwright, M. H. Choudhury, F. O. Afzal, T. Cao, S. I. Halimi, S. T. Retterer, I. I. Kravchenko, and S. M. Weiss, "Photonic crystal nanobeam biosensors based on porous silicon," Opt. Express 27(7), 9536–9549 (2019).
12. H. Inan, M. Poyraz, F. Inci, M. A. Lifson, M. Baday, B. T. Cunningham, and U. Demirci, "Photonic crystals: Emerging biosensors and their promise for point-of-care applications," Chem. Soc. Rev. 46(2), 366–388 (2017).
13. S. Bhattacharya and S. John, "Photonic crystal light trapping: Beyond 30% conversion efficiency for silicon photovoltaics," APL Photonics 5(2), 020902 (2020).
14. D. Zhou and R. Biswas, "Photonic crystal enhanced light-trapping in thin film solar cells," J. Appl. Phys. 103(9), 093102 (2008).
15. A. Chutinan, N. P. Kherani, and S. Zukotynski, "High-efficiency photonic crystal solar cell architecture," Opt. Express 17(11), 8871–8878 (2009).
16. S. Hu and S. M. Weiss, "Design of Photonic Crystal Cavities for Extreme Light Concentration," ACS Photonics 3(9), 1647–1653 (2016).
17. H. Choi, M. Heuck, and D. Englund, "Self-Similar Nanocavity Design with Ultrasmall Mode Volume for Single-Photon Nonlinearities," Phys. Rev. Lett. 118(22), 223605 (2017).
18. S. Hu, M. Khater, R. Salas-Montiel, E. Kratschmer, S. Engelmann, W. M. J. Green, and S. M. Weiss, "Experimental realization of deep-subwavelength confinement in dielectric optical resonators," Sci. Adv. 4(8), eaat2355 (2018).
19. D. P. Fromm, A. Sundaramurthy, P. J. Schuck, G. Kino, and W. E. Moerner, "Gap-dependent optical Coupling of Single "Bowtie" Nanoantennas in the Visible," Nano Lett. 4(5), 957–961 (2004).
20. D. R. Smith, W. J. Padilla, D. C. Vier, S. C. Nemat-Nasser, and S. Schultz, "Composite Medium with Simultaneously Negative Permeability and Permittivity," Phys. Rev. Lett. 84(18), 4184–4187 (2000).
21. J. Riedrich-Möller, C. Arend, C. Pauly, F. Mücklich, M. Fischer, S. Gsell, M. Schreck, and C. Becher, "Deterministic coupling of a single silicon-vacancy color center to a photonic crystal cavity in diamond," Nano Lett. 14(9), 5281–5287 (2014).
22. V. R. Almeida, Q. Xu, C. A. Barrios, and M. Lipson, "Guiding and confining light in void nanostructure," Opt. Lett. 29(11), 1209–1211 (2004).
23. J. D. Ryckman and S. M. Weiss, "Low mode volume slotted photonic crystal single nanobeam cavity in silicon," Appl. Phys. Lett. 101(7), 071104 (2012).